Charge sharing in common-grid pixelated CdZnTe detectors

Jae Cheon Kim *, Stephen E. Anderson, Willy Kaye, Feng Zhang, Yuefeng Zhu, Sonal Joshi Kaye, Zhong He

Department of Nuclear Engineering and Radiological Sciences, University of Michigan, Ann Arbor, MI 48109, USA

ARTICLE INFO

ABSTRACT

The charge sharing effect in pixelated CdZnTe (CZT) detectors with a common anode steering grid has been studied. The impact on energy resolution of weighting potential cross-talk and ballistic deficit due to cathode signal shaping has been investigated. A detailed system modeling package considering charge induction, electronic noise, pulse shaping, and ASIC triggering procedures has been developed to study the characteristics of common-grid CZT detectors coupled to the VAS_UM/TAT4 ASIC. Besides an actual common-grid CZT detector coupled to VAS_UM/TAT4 ASIC, a prototype digital read-out system has been developed to better understand the nature of the charge sharing effect.

© 2011 Elsevier B.V. All rights reserved.

1. Introduction

The pixelated CdZnTe (CZT) detectors using 3-D position-sensing techniques developed at the University of Michigan has demonstrated excellent energy resolution for gamma-ray spectroscopy and 4π Compton imaging capability [1]. It is known that the performance of pixelated CZT detectors is limited by several factors such as bulk and surface leakage currents, charge sharing, and charge transport non-uniformities [2]. In pixelated CZT detectors, multiple-pixel events consist of true Compton scattering and charge-shared events. The fraction of charge-shared events increases with the number of pixel triggered. It is reported that multiple-pixel events always have poorer energy resolution than expected based on the measured single-pixel event energy resolution and electronic noise [3]. Therefore, charge sharing is expected to be one of the primary factors to determine a pixelated detector's performance with respect to multiple-pixel events.

The 3-D position-sensing techniques enable multiple-pixel events of pixelated CZT detectors to be used for 4π Compton imaging. Multiple-pixel events occur by either multiple gamma-ray interactions or charge sharing from a single electron cloud between adjacent pixels. Charge-shared events happen when an electron cloud created underneath the gap between pixels is collected by more than one pixel. Each pixel must collect enough charge to pass a noise discrimination threshold. It is reported that

charge sharing in pixelated CZT detectors causes charge loss for events in the gap between pixels and degrades the performance of multiple-pixel events [4,5]. The charge sharing effect may vary according to several factors such as electron cloud size, pixel size, gap distance between pixels and the existence of a steering grid. The purpose of this work is to investigate the charge sharing effect for pixelated CZT detectors with a non-collecting steering grid (common-grid) through system modeling and measurement.

A non-collecting steering grid (common-grid) operated with negative bias surrounding the anode pixels has been known to improve the performance of pixelated CZT detectors [6]. A negative potential relative to the pixels on the non-collecting steering grid guides the electron clouds into the anode pixels for complete charge collection. A detailed simulation package has been developed to study the charge sharing effect within a common-grid pixelated CZT detector coupled to the VAS_UM/TAT4 ASIC. The simulation package considers gamma-ray interaction positions and energy depositions within the CZT crystal, electron drift trajectories, charge induction, electronic noise, pulse shaping, and ASIC triggering procedures. It is important to recognize that this work does not attempt a detailed simulation of the material defects or electric field non-uniformities commonly observed in CZT crystals [7]. While these factors have an important impact on the spectral performance of CZT, the purpose of this work is to understand the charge sharing effect for an ideal common-grid CZT detector system. In this way, fundamental and unavoidable problems due to the combination of charge transport, electrode configuration, and read-out technique are revealed.

---

* Corresponding author.
E-mail address: jaecheon@umich.edu (J.C. Kim).

The results of the system model are also compared with the measured data from an actual common-grid CZT detector system that uses a crystal manufactured by Redlen Technologies and the VAS_UM/TAT4 ASIC from Gamma-Medica-Ideas Inc. A prototype digital read-out system has also been devised to study the charge sharing effect. This system can estimate the interaction position with sub-pixel resolution and can isolate events occurring between pixels.

2. System modeling

2.1. Gamma-ray interaction and electron cloud model

GEANT4 [8,9] has been used to generate list-mode data containing gamma-ray interaction positions and energy depositions. For the GEANT4 simulation, the low-energy package is used with a 10 μm range cut-off for gamma-rays and a 1 μm range cut-off for electrons. Thus, gamma-rays and electrons are tracked until their kinetic energy drops below ~ 3 keV. Energy depositions are recorded in the case of photoelectric absorption, Compton scatter, and pair production, including the interactions of secondary photons such as characteristic X-rays and bremsstrahlung.

The mean electron cloud size at several gamma-ray energies has been calculated using GEANT4, as shown in Fig. 1. The mean electron cloud size was determined from the centroid of a Gaussian fitting curve of each distribution. When a ^{137}Cs gamma-ray energy is fully deposited in the CZT crystal, its mean electron cloud size has been calculated to be ~ 200 μm. The diameter of the initial electron cloud is determined by the two electrons that have the greatest separation distance, as shown in the insert of Fig. 1 (left). The electron positions are projected onto the x–y plane for determination of the electron cloud diameter.

Due to random thermal motion of electrons, the electron cloud expands as it drifts. Thus, the spread, s, due to diffusion is approximated by a Gaussian distribution:

$$FWHM(s) = 2.35\sqrt{\frac{2kTdD}{eV}} = 0.529\sqrt{\frac{dD}{V}} \qquad (1)$$

where k is the Boltzmann constant, T (293 K) is the absolute temperature, d is the drift distance, D (15 mm) is the detector thickness, e is the unit charge and V (-3000 V) is the cathode bias. If a ^{137}Cs gamma-ray energy is fully deposited at the cathode side of detector, the initial electron cloud size and the spread due to diffusion are ~ 200 and ~ 150 μm, respectively. The electron cloud size will expand to $\sqrt{200^2 + 150^2} = \sim 250$ μm after drifting through the entire thickness of the crystal. It is known that the increase of electron cloud size due to Coulomb repulsion between electrons is relatively small compared to the increase by diffusion [10]. Therefore, in this simulation, the Coulomb repulsion force between electrons is not considered. For simplicity, the model assumes that electron clouds have a plane circular shape without extent in the depth dimension.

2.2. Charge transport and induction model

The anode array pattern, applied to a CZT crystal with dimensions of 20 mm × 20 mm × 15 mm, includes an 11 × 11 square pixel array fabricated on the anode surface with a pixel pitch of 1.72 mm, as shown in Fig. 2. Charge induction in pixelated CZT detectors is primarily determined by the weighting potential distribution along the drift trajectory of electrons.

Fig. 3 shows the weighting potential as a function of depth along lateral positions from #1 to #3, generated by MAXWELL3D [11], for the pixelated CZT detector with a steering grid. In order to model electron and hole trapping in CZT grown by Redlen Technologies, a mobility-lifetime of 3.00×10^{-2} cm^2/V was used for electrons and a mobility-lifetime of 1.50×10^{-4} cm^2/V was used for holes [12].

A steering grid is used to focus electron clouds into the anode pixels. While the common-grid improves the measured performance, it introduces several modeling difficulties. In general, the electron clouds created in pixelated CZT detectors without a steering grid are expected to drift along a straight line from the cathode toward the anode. However, if a common-grid is used to steer electron clouds into the pixels, a curved drift trajectory should be considered for calculation of charge induction, as
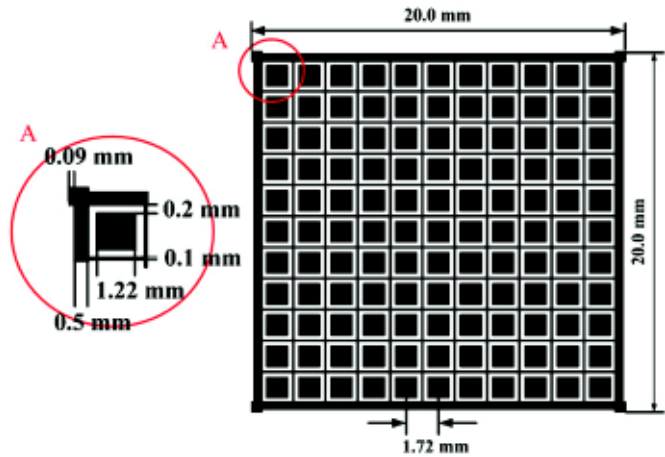

Fig. 2. Anode design of modeled pixelated CZT detector with a non-collecting steering grid (common-grid).
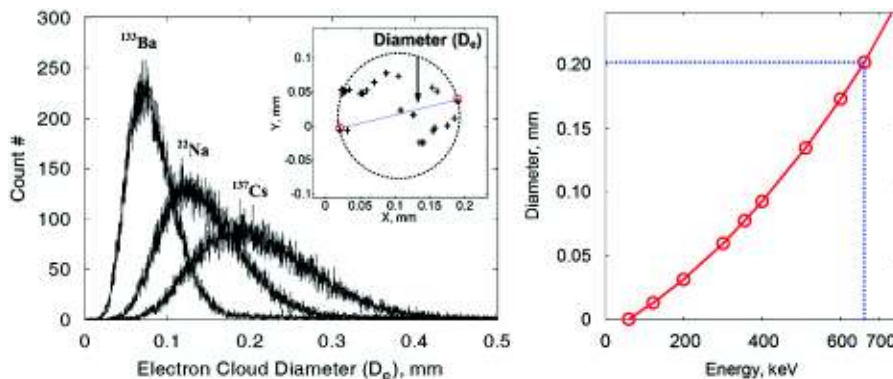

Fig. 1. Determination of electron cloud diameter based on the two electrons that have the greatest separation distance and the distribution of electron cloud diameters.
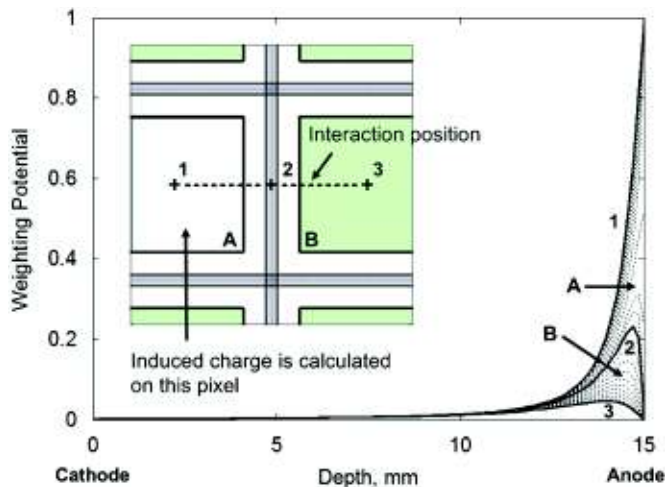
Fig. 3. Weighting potential distribution for the pixel A as a function of depth underneath different lateral positions (1, 2, or 3 in the inset diagram).
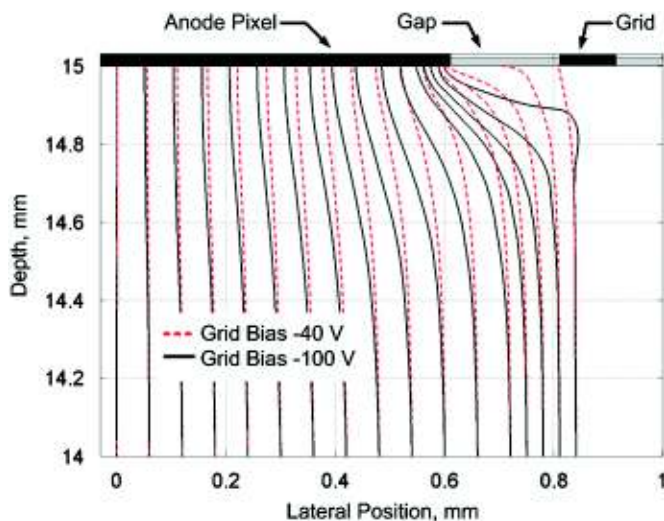

Fig. 5. The variation of weighting potential along the electron drift trajectories with a grid bias of 0, −40, and −100 V for the same lateral position of interaction.

Fig. 4. Electron drift trajectories for grid bias voltages of −40 and −100 V and different lateral interaction positions.

shown in Fig. 4. Fig. 5 shows the variation of weighting potential along electron drift trajectories at different grid bias values, for gamma-ray interactions underneath the gap between pixels. A steering grid enables most of the electron clouds created underneath the gap to be effectively collected by the pixels. In order to consider the statistical fluctuation in the charge carrier creation, a Fano factor of 0.1 has been applied to simulation model [3].

2.3. ASIC read-out system

The VAS_UM/TAT4 ASIC chip is used to read-out both the amplitude of charge induction and the electron drift time independently for each anode pixel [3]. The ASIC has 128 channels, each with a charge-sensitive preamp and two CR-RC unipolar shapers with different shaping times. The slow shaper has 1-μs peaking time and is coupled to a peak-hold stage to record pulse amplitude. The fast shaper has a 100-ns shaping time and is coupled to simple level discriminators for timing pickoff. One hundred and twenty one channels are connected to the pixels, 1 channel is connected to the grid, and 1 channel is connected to the cathode. Compared to the anodes, the polarity of the signals are reversed for the cathode and grid. The peak-hold properties,
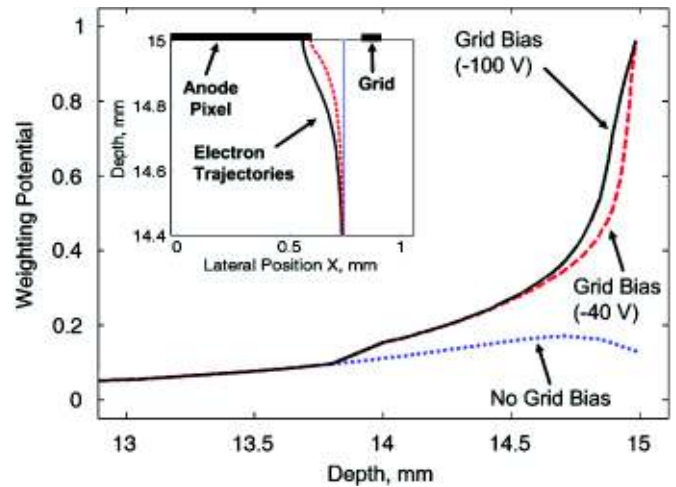
signal shaping, ASIC noise, and triggering procedures are included in the ASIC read-out system model. The fast shaper can trigger off pulses as small as 30 keV for the anode and 50 keV for the cathode. Only the pixels with slow shaped signals greater than a noise discrimination threshold of 25 keV were considered. The method of Pullia and Riboldi is employed to simulate the ASIC electronic noise in a detector system [13]. The amplitudes of the electronic noise on each anode pixel and the cathode are assumed to be 3 keV FWHM and 20 keV FWHM respectively based on recent experimental measurements using the VAS_UM/TAT4 ASIC.

Fig. 6 shows typical simulated fast and slow shaped signals for the anode and cathode coupled to the VAS_UM/TAT4 ASIC. The AVA and CVA are the maximum amplitude of the slow shaped signals of the anode and cathode. The drift time of electrons was determined from the time interval between the anode and cathode timing signals obtained from the leading edge of the fast shaped signals.

In order to investigate the impact on energy resolution of ballistic deficit for the cathode, an additional model that does not use signal shaping (IDEAL SHAPING MODE) has been considered. In this mode, the pulse heights are determined based on the maximum values of the preamp signals without noise, to reflect ideal shaping. The system noise contribution is added at the end of the pulse height determination process. In Fig. 7(b), the ballistic deficit does not exist, as the AVA and CVA are directly obtained from the value of the preamp signal 1-μs after the gamma-ray interaction occurs, rather than the maximum amplitude of the slow shaped signals in the VAS_UM/TAT4 ASIC. The drift time of electrons is obtained from the fast shaped signals in the same way as the VAS_UM/TAT4 ASIC.

3. Charge sharing in common-grid detectors

In an ideal pixelated CZT detector, charge sharing caused by splitting the electron cloud between pixels is an important mechanism that degrades the performance of multiple-pixel events. Theoretically, split electron clouds are expected to be fully collected into the neighboring pixels in common-grid detectors. However, the weighting potential cross-talk between pixels increases as the gamma-ray interaction occurs closer to the pixel boundary. Charge induction from interactions underneath the gap between pixels can be smaller than in the central area of each pixel, even if the split electron clouds are fully collected into the
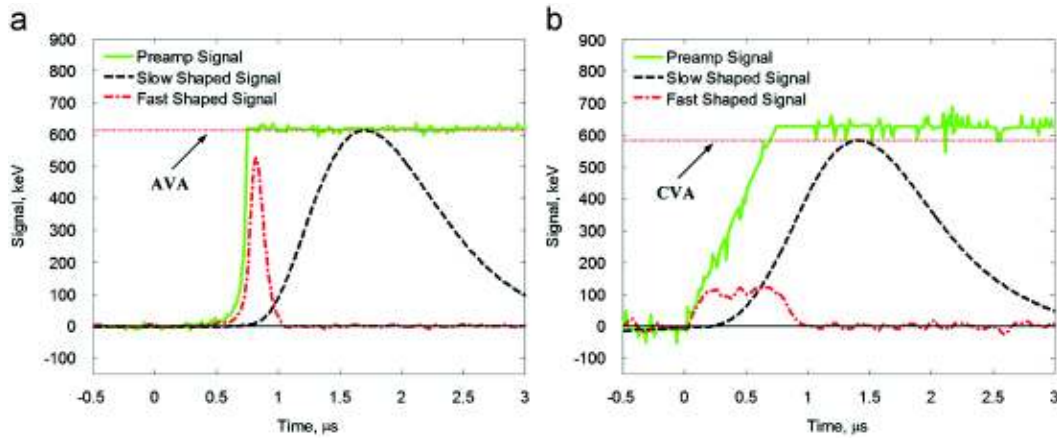
Fig. 6. Typical simulated fast and slow shaped signals for the (a) anode and (b) cathode based on parameters of the VAS_UM/TAT4 ASIC. For convenient comparison between anode and cathode signals, the value of cathode signals is multiplied by −1.
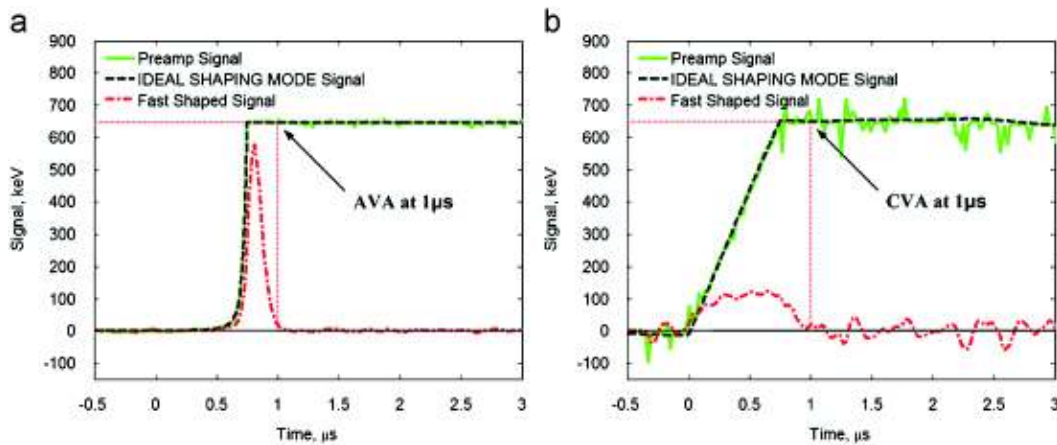

Fig. 7. IDEAL SHAPING MODE signals for the (a) anode and (b) cathode that artificially eliminates the ballistic deficit due to signal shaping in the VAS_UM/TAT4 ASIC. For convenient comparison between anode and cathode signals, the value of cathode signals is multiplied by −1.

pixels. This is because the transient signal induced in the neighboring pixels always results in negative net charge induction, therefore, if this neighbor pixel also collects some charge the signal amplitude will be diminished. In the most extreme case, electron clouds occurring underneath the gap between pixels cause the side-by-side pixels to have relatively large reciprocal transient signals that reduce the signal magnitude in each pixel. Charge-shared events always experience charge loss due to reciprocal transient signals between pixels, which will be referred to as weighting potential cross-talk. Therefore, an accurate charge induction model considering weighting potential cross-talk caused by the movement of an electron cloud in the neighboring pixels is critical to understand the energy resolution degradation in multiple-pixel events.

3.1. Simple charge sharing model

A charge sharing model is required to simulate the interactions that occur in the gap between pixels in common-grid detectors. When the gamma-ray energy is collected by the central area of each pixel without charge sharing, the electron cloud is considered as a single point. In this case, the charge induction in the collecting pixel and transient signals in the neighboring pixels are easily calculated according to the weighting potential difference. However, when the electron cloud is created below multiple pixels, as shown in Fig. 8, the weighting potential cross-talk caused by each shared electron cloud should be considered,
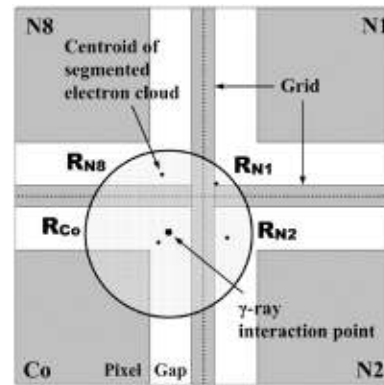

Fig. 8. The simple charge sharing model that separates a single charge sharing interaction into multiple non-charge sharing events.

individually. In the pixel Co in Fig. 8, a final charge induction Q_c can be calculated using the following equation:

$$Q_c = (R_c W_c^c + R_1 W_1^c + R_2 W_2^c + R_8 W_8^c) \times Q_t \tag{2}$$

where Q_t is the total deposited energy and R_c, R_1, R_2, and R_8 are the deposited energy fractions in each pixel. In Eq. (2), W_c^c is the fractional charge induction in pixel Co by the charge cloud located in pixel Co while W_1^c is the fractional charge induction in pixel Co by the charge cloud located in pixel N1. W_1^c, W_2^c, and W_3^c always

have either zero or negative values. Therefore, the total charge induction Q_c considering weighting potential cross-talk is always smaller than the one in the central region of pixel without charge sharing. In order to evaluate an impact of weighting potential cross-talk, the WPCT OFF MODE that artificially eliminates the weighting potential cross-talk in charge-shared events like W_1^c, W_2^c, and W_3^c is added in the simulation. A final charge induction in the pixel Co not considering weighting potential cross-talk can be calculated using the following equation:

$$Q_c = R_c W_c^c \times Q_t. \tag{3}$$

3.2. Energy resolution degradation

The weighting potential cross-talk caused by charge-shared events is a major factor that can degrade the energy resolution of pixelated CZT detectors with a steering grid if the material defects or electric field non-uniformities commonly observed in real CZT crystals are not considered. In this study, only ideal pixelated CZT detectors are simulated to reveal the fundamental problems due to the combination of charge transport, electrode configuration, and read-out technique. Using this ideal model, the energy resolution for 1-, 2-, 3-, and 4-pixel events after complete system calibration has been calculated. Simulated results have been compared with measurements from an actual common-grid detector system. As introduced in the previous section, the IDEAL SHAPING MODE and the WPCT OFF MODE have been considered to evaluate an impact on energy resolution of ballistic deficit in the cathode signal and weighting potential cross-talk in charge-shared events.

In a real detector system, the impact of charge sharing is difficult to isolate from other factors. This makes simulation an excellent choice for studying these effects; in addition to the WPCT OFF MODE it is possible to completely eliminate the contribution from charge sharing events by rejecting gamma-interactions occurring under the gap between pixels. A special data set (NO GAP MODE) excluding the events that interact more than 0.7 mm away from each pixel center has been prepared. If the primary cause of energy resolution degradation in charge-shared events is weighting potential cross-talk then NO GAP MODE and WPCT OFF MODE should yield similar results.

The measured energy spectra from an actual common-grid CZT detector system coupled to a VAS_UM/TAT4 ASIC are compared to simulation. The charge collection and energy spectrum have been simulated based on ^{137}Cs gamma-ray 3D interaction position (x,y,z) and energy deposition data from GEANT4. In the simulation, the detector is assumed to be uniformly irradiated by ^{137}Cs gamma-rays

from the cathode side. Fig. 9 shows a single-pixel (left) and two-pixel (right) energy spectra from measurement and simulation. The energy resolution values from the simulated ideal detector are expected to be much better than the measured ones. This is because several factors such as material defects and charge transport non-uniformity that can significantly affect the energy resolution are not considered in the ideal detector model.

If 3 keV ASIC electronic noise for the anode is the only factor that determines the system performance, the expected energy resolutions for 1-, 2-, 3-, and 4-pixel events are 0.45%, 0.64%, 0.78%, 0.91%, respectively. When several factors such as cathode ASIC electronic noise, ballistic deficits due to signal shaping, and weighting potential cross-talk are considered, 0.53% and 0.76% were calculated as the theoretical limit of energy resolution for 1- and 2-pixel events in the modeled detector system. Despite the differences between measurement and simulation, the ideal detector model is still very useful to understand the characteristics of detector system including its theoretical performance limits. In order to properly operate and calibrate the system the ideal behavior must be understood first. Otherwise, it will be very challenging to correlate system performance to detector quality and to develop proper calibration techniques for the important effects evident in the ideal behavior, such as charge induction or ASIC timing pickoff.

Fig. 10 shows the energy resolution for 1-, 2-, 3-, and 4-pixel events of simulations after complete system calibration. The ideal detector model is used to compare the energy resolution degradation between other simulation modes. As a result, a magnitude of energy resolution degradation due to ballistic deficit and weighting potential cross-talk was ∼5% to ∼9%. The energy resolution of special data set excluding the gap events (NO GAP MODE) was similar with the one of IDEAL SHAPING MODE and WPCT OFF MODE while its photopeak counts significantly decrease with the number of pixels triggered. In the measurement, the number of events with at least 1 side neighbor interaction are at least ∼15 times larger than the non-side neighbor events in the 4-pixel events as shown in Table 1. However, in the NO GAP MODE, the number of side neighbor events that include charge-shared events are only ∼4 times larger than the non-side neighbor events. This means that the probability of a 4-pixel event with charge sharing significantly decreases with reduction of the side neighbor events through elimination of charge-shared events in the gap between pixels. The fact that the NO GAP MODE performance is very similar to the WPCT OFF MODE indicates that the dominant cause of energy resolution degradation in charge-shared events is due to the weighting potential cross-talk. The slight improvement in the
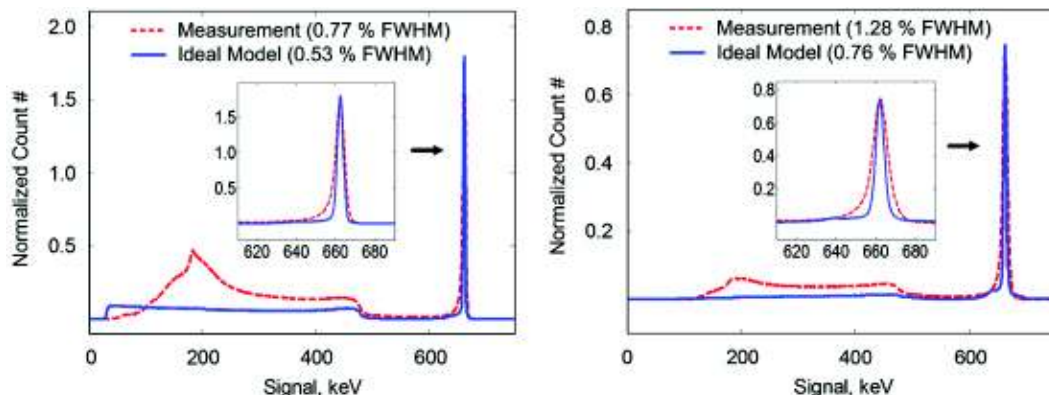

Fig. 9. The simulated and measured energy spectra for single-pixel (1-px) and two-pixel (2-px) events when a ^{137}Cs gamma-ray is incident on the cathode. Measurements have been performed with a common-grid CZT detector (4R60) coupled to a VAS_UM/TAT4 ASIC.
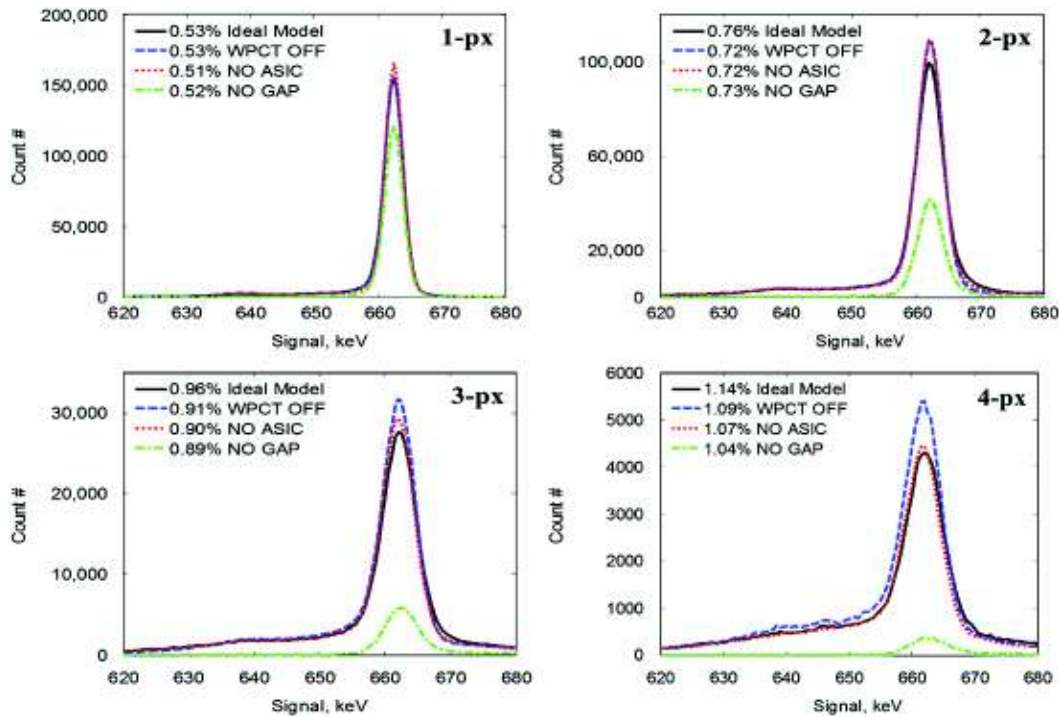
Fig. 10. Comparison of FWHM energy resolution between the ideal model and three different MODEs (WPCT OFF MODE, IDEAL SHAPING MODE, and NO GAP MODE) for 1-, 2-, 3-, and 4-pixel events.

Table 1

Simulated and measured event fraction for non-side neighbor (NN) and side neighbor events (SN) when 662 keV gamma-rays (^{137}Cs) are incident on the cathode. Simulated side neighbor events are divided into Compton scatters (Comp) and Charge-shared events (ChSh). Both simulated and measured statistical uncertainties are less than $\sim 0.002\%$.

Method	Event type	1-px (%)	2-px (%)	3-px (%)	4-px (%)
Simulation	Photopeak	38.2	42.1	16.3	3.4
	NN	–	21.7	3.9	0.3
	SN	–	20.4	12.4	3.1
	(Comp)	–	(15.5)	(6.8)	(1.3)
	(ChSh)	–	(4.9)	(5.6)	(1.8)
Measurement	Photopeak	35.5	43.6	17.2	3.7
	NN	–	19.0	3.1	0.2
	SN	–	24.6	14.1	3.5

NO GAP MODE data relative to the WPCT OFF mode data can be credited to effects such as a smaller variation in weighting potential at each depth as the limited interaction locations have restricted the active area of each pixel.

3.3. Event fraction

The probability of charge sharing is a function of the lateral position of gamma-ray interactions and the size of the electron cloud when it reaches the pixel. Fig. 11 shows the depth and distance from the pixel center where charge sharing will begin to take effect for several energies, considering all the properties of the modeled common-grid pixelated CZT detector system. Between each line of onset and the pixel boundary, all of the interactions trigger the side-neighboring pixel as well as the collecting pixel. This onset look-up table is used to distinguish charge-shared events from Compton scatters between side-neighboring pixels for the 2-, 3-, and 4-pixel events.
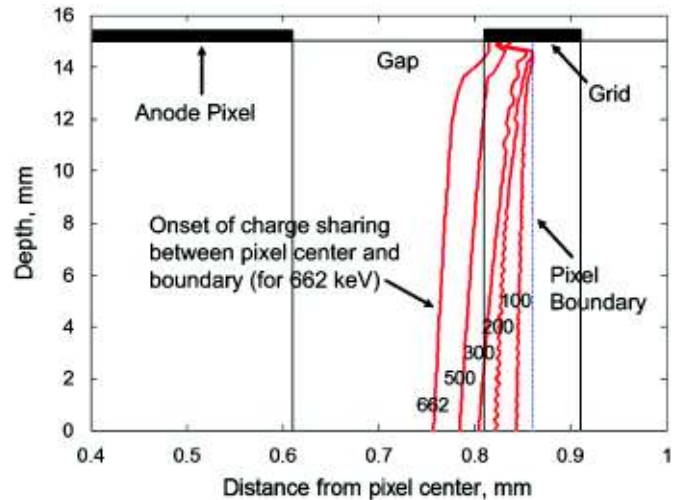

Fig. 11. The furthest lateral position from the grid where charge sharing is possible at each depth as a function of the deposited energy in a common-grid detector, results are calculated from simulation.

Table 1 shows the event fractions determined by the photopeak events of the ideal model and the measurement. The photopeak events are primarily used for calibration of an actual detector system. In measurement, the multiple-pixel events are divided into non-side neighbor (NN) and side neighbor (SN) events. Below 1 MeV, the non-side neighbor events are due to Compton scatters (Comp). But side neighbor events can involve either Compton scattering or charge sharing (ChSh). As shown in Table 1, the ratio of side neighbors to non-side neighbors significantly increases with the number of pixel triggered. The number of 2-pixel side neighbor events is similar to the number of non-side neighbor events. However, the side neighbor events become ~ 4 times and ~ 15 times more probable than the non-side neighbor events in 3- and

4-pixel events. Among side neighbor events, charge-shared events are more likely to contributes to energy resolution degradation than Compton scattering events, in part because this represents the most extreme case of weighting potential cross-talk. Among the side neighbor events, the fraction of charge-shared events is at most ∼1.4 times larger than the fraction of Compton scattering events, increasing with the number of pixels triggered. The significant increase in the relative fraction of charge sharing to true Compton scatters in the side neighbor events is one important factor that causes the energy resolution degradation in multiple-pixel events.

3.4. Two-Pixel side neighbor events

It is important to understand the details of the mechanism by which charge sharing degrades the energy resolution. There are several possible outcomes when an electron cloud is near the gap between pixels. Charge induction from split electron clouds could all be bigger than the ASIC triggering threshold and the charge cloud in each pixel would contribute to recorded energy. Another case is when both pixels collect some charge, but only one pixel has a large enough signal to be considered a true energy deposition, which is based on the noise discrimination threshold of the system. In this case the recorded energy will be too small because the contribution from part of the electron cloud is not considered. In the final case the charge is entirely collected by one pixel, but the electron cloud induces a transient signal on a neighbor pixel that is sufficient to pass the noise discrimination threshold after shaping and peak hold. In this case the recorded energy will be too large, as a false signal induction on a neighbor pixel is considered in addition to the complete charge collection by one pixel. An accurate model of ASIC signal shaping and triggering procedures is required to understand the impact of these effects on pixelated CZT detectors.

Fig. 12 shows the impact of the reciprocal weighting potential cross-talk between two side-neighboring pixels through use of WPCT OFF MODE. The uncorrected signals have been calibrated by the signal from 1-pixel events at the same depth but located in the center point of the pixel. When the transient signals are not considered, the signal amplitude can be fully recovered to the original energy deposition. However, when the transient signals are considered, the reconstructed signals are not fully recovered. The maximum signal loss occurs directly below the steering grid. As discussed earlier, it is possible that a neighbor pixel passes the system noise discrimination threshold without actually collecting any charge. This can be seen in Fig. 12 for the events in the middle of the gap between the grid and each pixel, ∼0.1 mm away from the center of steering grid. It is clear that for these events the total signal amplitude is larger than the expected photopeak signal amplitude.

In a pixelated CZT detector with a simple-pixel anode array pattern, the charge sharing effect has been studied as a function of the inter-pixel gap size [4]. It has been reported that there is some signal loss due to charge-shared events between pixels in simple-pixel CZT detectors. In order to investigate the effect of charge sharing effect among side neighbor events in common-grid CZT detector coupled to an ASIC, the reconstructed 2-pixel events after complete system calibration were collected from the same simulation and measurement data shown in Fig. 9. The total signal amplitude Q_T and the signal ratio of two pixels L_T were calculated using the following equation:

$$Q_T = S_A + S_B, \quad L_T = \frac{S_A - S_B}{S_A + S_B} \tag{4}$$

where S_A and S_B are the signal from pixel A and B, respectively.

Fig. 13 shows the reconstructed 2-pixel side neighbor and non-side neighbor events as a function of the signal ratio and the total signal amplitude from simulation. The WPCT OFF MODE is the ideal model excluding the weighting potential cross-talk. The WPCT ON MODE is the same as the ideal model used in Fig. 9. The results show that the weighting potential cross-talk has a much stronger impact on side neighbor events than non-side neighbor events, as expected. In Fig. 14, the measurement performed by the actual common-grid detector system shows similar features observed in the simulation, such as the increase in the total signal when the signal is almost entirely collected by
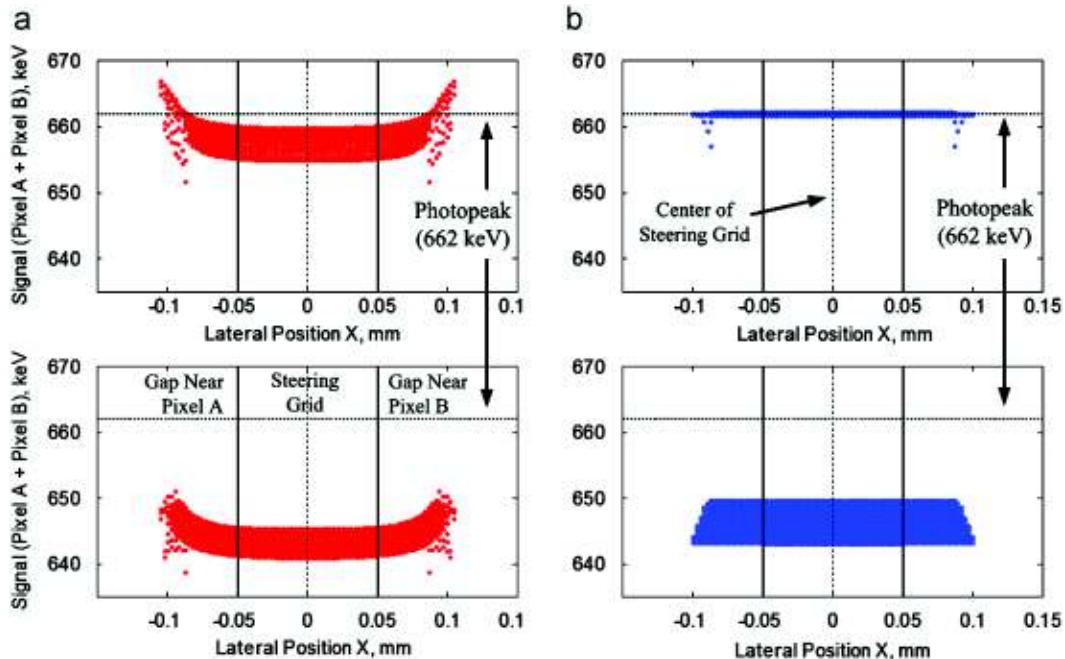

Fig. 12. The uncorrected (bottom) and corrected (top) signals as a function of lateral positions calculated by the ideal model with (left) and without (right) weighting potential cross-talk. The total signal is calculated by the summation of pixel A and pixel B. The gamma-ray depths of interaction are distributed uniformly within 10 mm of the cathode side. ASIC noise is not considered.
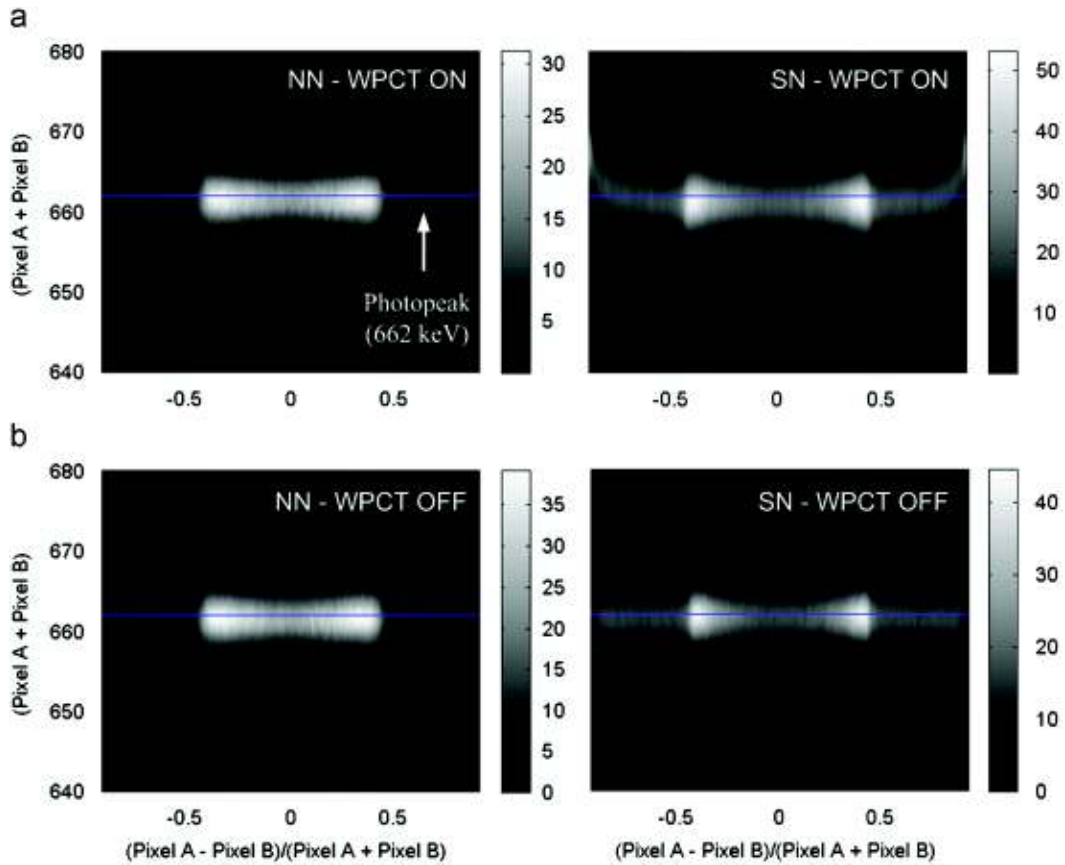
Fig. 13. The reconstructed 2-pixel side neighbor and non-side neighbor events as a function of the lateral position and the total signal amplitude collected using WPCT ON MODE (a) and WPCT OFF MODE (b). The non-side neighbor events (NN) are on the left. The side neighbor events (SN) are on the right.
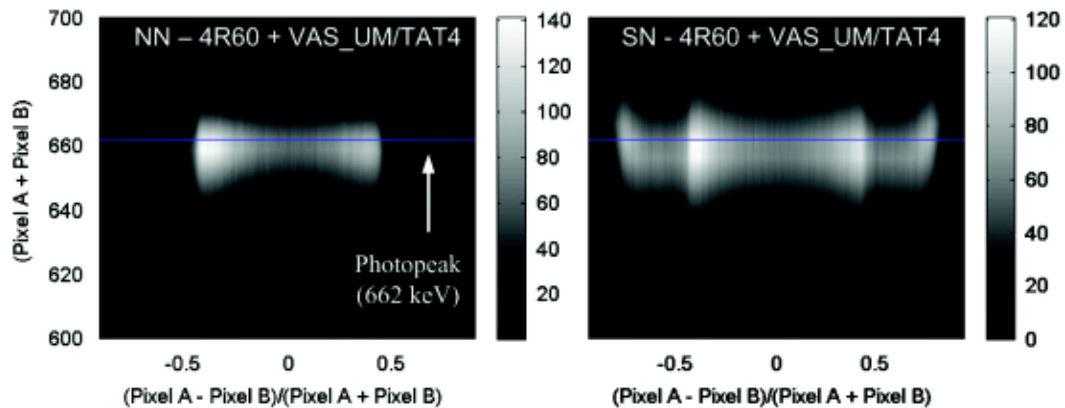

Fig. 14. Measured data showing reconstructed 2-pixel side neighbor and non-side neighbor events as a function of the lateral position and the total signal amplitude collected from the ideal model and the measurement in Fig. 9.

one pixel. If only measured data were available, this observation could easily be confused with other effects, such as nonlinearity in the preamplifiers.

4. Charge sharing studied by a digital read-out system

4.1. Sub-pixel interaction position

The experimental results from the common-grid detectors coupled with the VAS_UM/TAT4 ASIC have demonstrated that the simulation model as a whole is an accurate representation of the physical system. However, in order to experimentally analyze

the more detailed detector behavior such as charge sharing, a prototype digital read-out system has been developed for pixelated CZT detectors [14]. This digital system experimentally provides advanced sub-pixel interaction position as well as signal pulse waveform data as in the simulation.

The connection between charge sharing and energy resolution of both single- and multiple-pixel events can be studied experimentally using the sub-pixel interaction position estimates. As shown in Fig. 15, the lateral interaction position within a single pixel can be calculated using analysis of the charge induction signals from pixels that neighbor the pixel under which the interaction takes place [15]. Even when charge is not collected by a neighboring pixel, the movement of electrons in the

collecting pixel volume induces a signal waveform. These non-collecting neighbor signals are referred to as transient signals. For a given amount of charge following an interaction, the amplitude
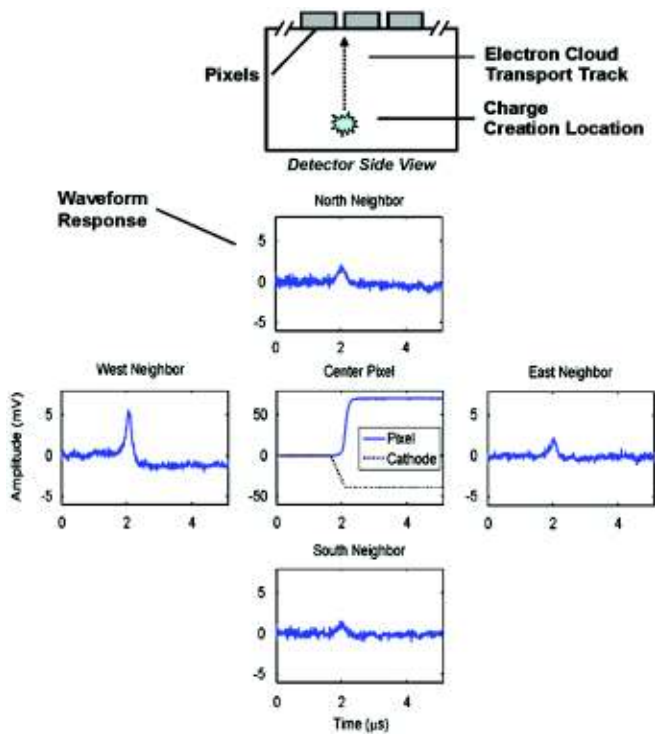

Fig. 15. The unshaped charge signals of pixels on the border of electron-collecting pixels that contain information related to the lateral position of the charge cloud.

of a neighbor transient signal depends on where the interaction takes place in the collecting pixel. The maximum transient amplitude occurs when the electron cloud is created on the side of the collecting pixel that is closest to this particular neighbor. The minimum transient amplitude occurs when the interaction occurs on the opposite side of collecting pixel.

A uniform electron cloud with a centroid in the middle of a pixel would induce identical transient signals on its four cardinal neighbors. When the centroid of the electron cloud is not in the center of the pixel, the transient signals from neighbors nearest to the centroid will have larger amplitudes than their opposing neighbors. The difference in relative transient signal height is used to reconstruct sub-pixel position from the acquired waveforms. In this study, sub-pixel position ratios R_x and R_y are defined as

$$R_x = \frac{S_W - S_E}{S_W + S_E}, \quad R_y = \frac{S_N - S_S}{S_N + S_S} \qquad (5)$$

where S_W, S_E, S_N, and S_S are the transient pulse heights from neighboring pixels surrounding the collecting pixel. In order to estimate the x lateral sub-pixel position, the transient heights from the east and west neighboring pixels S_W and S_E are used. The north and south transient amplitudes S_N and S_S would provide the y lateral position. These ratios are then correlated to real sub-pixel locations providing the basis for sub-pixel analysis.

4.2. Experimental setup

A prototype digital read-out system has been developed for the sub-pixel experiment. Fig. 16 (top) is a picture of the top and bottom of the board. The detector dimensions are identical to the detector used in simulation. The detector is manufactured by eV products. Only 16 read-out channels are available with this
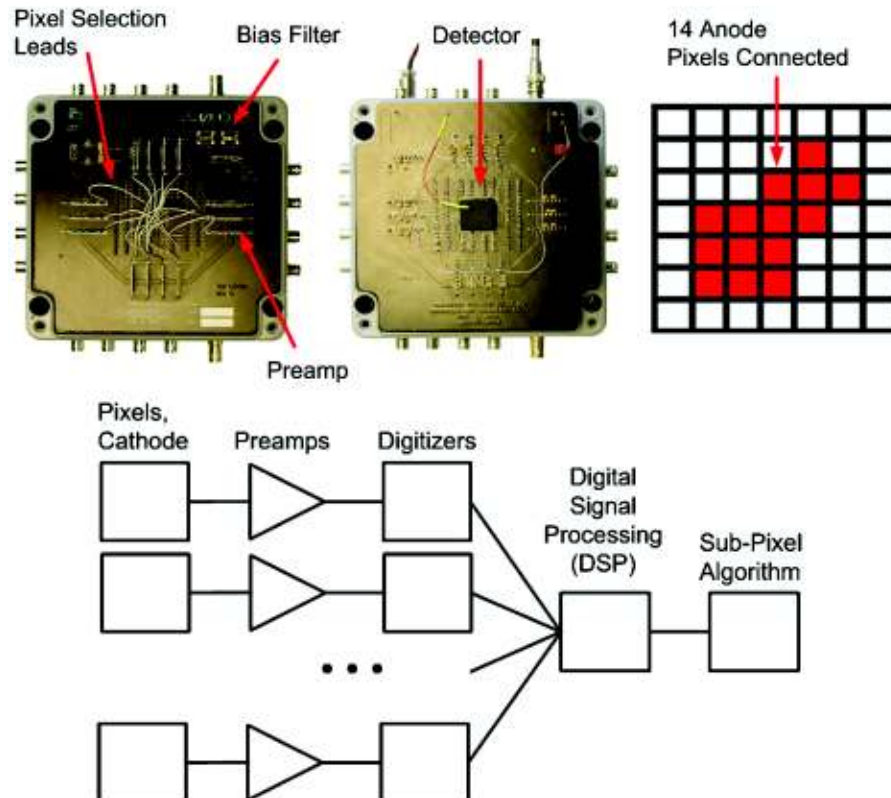

Fig. 16. The prototype digital read-out system (top) and the data collection procedures (bottom) for the sub-pixel interaction experiment. This arrangement is different from the analog ASIC because unshaped pixel and cathode pulse waveforms are digitized for subsequent-software-based analysis.

system, thus 14 channels are connected to anode pixels, 1 channel is connected to the grid, and 1 channel is connected to the cathode, as shown in Fig. 16. The anode (pixels) and cathode signals first pass through preamplifiers (model eV-5093). The preamplifier signals are digitized using PCI-based GaGe Octopus Compuscopes (Model OCT-838-009). Each card has eight 14 bit channels that can sample at rates up to 125 MS/s (>100 MHz bandwidth). The digitized waveforms then pass into a computer where the signals are processed to obtain pulse heights and timing information for various waveform features. Using sub-pixel position algorithms, a more accurate sub-pixel interaction location was determined inside the collecting pixel for each gamma-ray interaction.

4.3. Elimination of charge-shared events

Neighbor transient signals can be used to determine interaction locations in sub-pixel regions within a pixel. This function can enable us to discriminate events according to sub-pixel position. Fig. 17 shows two ^{137}Cs spectra from the same pixels after the depth-dependency due to charge trapping and weighting potential is eliminated by applying a depth-correction.

The spectrum represented by the solid line is from interactions that occur in the entire volume of a single pixel. This volume is defined by the detector thickness, and laterally by the pixel pitch. The spectrum represented by the dashed line is from interactions that occur in a volume defined by the entire detector thickness, but laterally constrained to the center region of a single pixel. The center region is determined using the transient signal ratios defined in Eq. (5). Knowing that R_x and R_y are bound between

-0.5 and 0.5 for single pixel events at 662 keV, the center region is defined as $|R_x|\&|R_y| > 0$, $|R_x|\&|R_y| < 0.25$. The photopeak areas of the spectra in Fig. 17 have been normalized to allow a direct comparison of the 662 keV photopeak amplitude in the different pixel regions.

The amplitude of transient pulses is closely related to the initial number of electrons in the collecting pixel and the sub-pixel interaction position. The closer the interaction occurs to the edge of pixel, the larger the transient signal will be in the neighboring pixel. In Fig. 17, the Compton continuum of the spectrum from the pixel center (dashed line) has fewer counts than the full-pixel spectrum (solid line). This is because interactions in the center of the pixel tend to generate smaller transient signals on the neighbor pixels, which are more difficult to identify at the relatively low energies of the Compton continuum. Both spectra in Fig. 17 show a reduction in events below 200 keV and very few below 100 keV since the method performs poorly below this energy. The event trigger threshold of the experiment was 30 keV on the collecting pixel anode.

In the context of this work, the most interesting difference between these spectra occurs in the photopeak region. The first difference can be found in the low-energy photopeak tails. In the pixel-center spectrum, there are fewer events in the low-energy tail region compared to the full-pixel spectrum. This is consistent with the observation that photopeak low-energy tailing in a pixelated detector comes from interactions in the gap between pixels. This agrees with simulation results. Events from interactions occurring in the center of a pixel are the least likely to share or lose charge, assuming the size of the electron cloud is smaller than the pixel size. The full-pixel spectrum has more counts in the low-energy tail because it includes events near the pixel edge where charge can be shared to other pixels or lost to the gap. While the FWHM at 662 keV of the full-pixel spectrum is 0.65%, it is improved to 0.58% in the center-pixel spectrum. In this way, calibration methods based on the sub-pixel interaction positions can improve overall energy resolution by accounting for charge sharing and loss for events near a pixel edge.

Another way of using sub-pixel position estimates to understand the relationship between charge sharing and interaction location is to calculate the interaction position of suspected charge-shared events from an energy spectrum. Fig. 18 shows the sub-pixel interaction distribution of three different energy windows for the entire full-pixel photopeak in Fig. 17. The interaction positions in these distributions are binned in two dimensions as a function of transient signal ratios. The ratios as calculated using Eq. (5) fall between -1 and 1 in both the x and y directions. The ratio values that correspond to the edge of a pixel depend on the energy-dependent size of the electron cloud. At 662 keV, the ratio values that correspond to the edge of a pixel are near -0.5 and 0.5. The middle of a pixel would be at ratios of 0. As expected, since the pixel has been uniformly irradiated, the
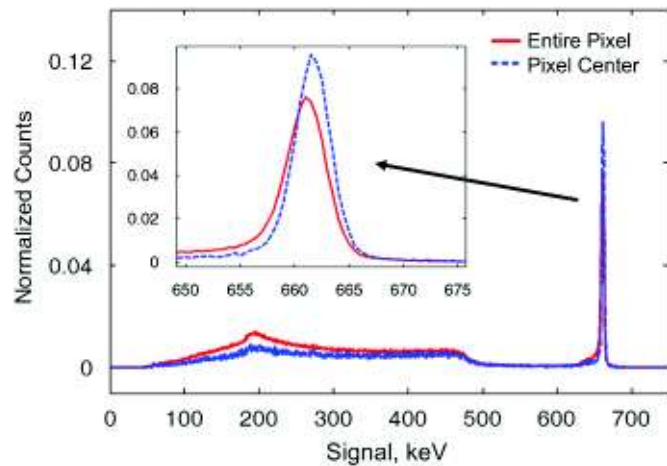

Fig. 17. Comparison of ^{137}Cs spectra from single-pixel events that interact in the middle of a pixel and throughout the entire pixel. Counts in each spectra have been scaled to normalize the two photopeak areas.
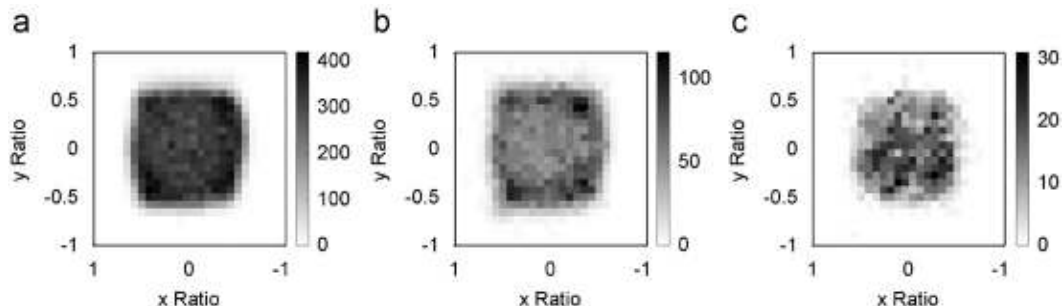

Fig. 18. Comparison of sub-pixel interaction position for three different energy windows: the entire photopeak (left), the low-energy tail (middle), and the high-energy photopeak side (right). The intensity bar indicates the number of counts per 2-D bin.
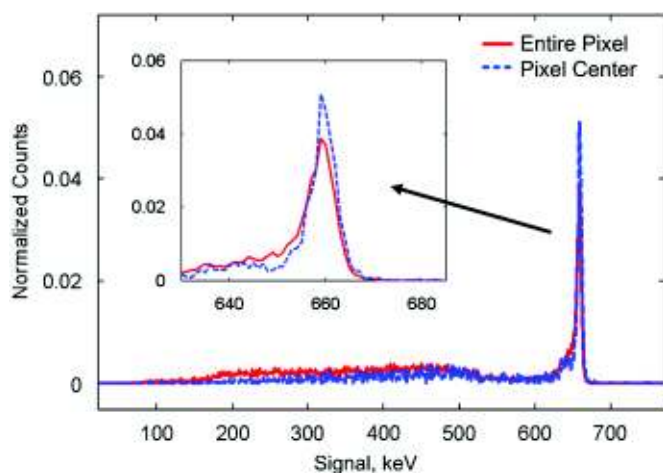
Fig. 19. Comparison of ^{137}Cs spectra from two-pixel events between two non-neighboring pixels. The spectrum of events interacting in the centers of the pixels is compared to the spectrum due to events interacting in the entire pixel volumes.

interaction distribution is uniform between the pixel boundaries in Fig. 18(a). The interaction distribution for events selected from the low-energy tail of the photopeak is shown in Fig. 18(b). This distribution is biased toward interaction locations near the edge of the pixel. This distribution is consistent with the sub-pixel regions where charge sharing and gap-related loss are most likely. Likewise, Fig. 18(c) illustrates the pixel-center biased distribution of events selected from the highest energy bins of the photopeak. The highest energy photopeak counts come from events that occur in the center of the pixel, while the lowest energy photopeak counts come from events occurring near the pixel edge.

Sub-pixel interaction position estimates can also be used to study the effect of charge sharing on multiple-pixel events. Fig. 19 shows depth-corrected spectra from two-pixel events of non-neighboring pixels. A Compton scatter between two pixels is an example of the type of event that makes up this spectrum. In Fig. 19, the solid line includes scatters between any interaction location in the first pixel to any interaction location in the second pixel. The second spectrum (dashed line) includes scatters from interactions in the center region of the first pixel to an interaction in the center of the second pixel. When the two interactions occur in the center region of each pixel, the photopeak resolution (FWHM at 662 keV) is 0.79% compared to 0.99% for full-pixel interaction events. As in the case of single-pixel events in Fig. 17, the low-energy tail of the pixel-center spectrum is smaller than the full-pixel spectrum.

5. Discussion

A signal modeling package and a prototype digital read-out system have been developed for the analysis of charge sharing in pixelated CZT detectors with a steering grid coupled to the VAS_UM/TAT4 ASIC. This tool has been used to investigate the impact of weighting potential cross-talk due to charge-shared events, ballistic deficit and the energy resolution degradation of multiple-pixel events observed in the experimental results. Using sub-pixel position estimates, a prototype digital read-out system can experimentally show the underlying causes behind the energy resolution degradation in single- and multiple-pixel events due to charge sharing. The photopeak tail of single-pixel events has been shown to be due, in part, to signal loss to a neighbor pixel that is too small to pass the noise discrimination threshold.

In an ideal common-grid detector system, both the weighting potential cross-talk due to charge-shared events and ballistic

deficit due to signal shaping in the cathode are factors that degrade the energy resolution by $\sim 6\%$ to $\sim 8\%$ for multiple-pixel events. The probability of charge sharing occurring in a side neighbor event increases rapidly with the number of pixel triggered. This is one of the reasons why energy resolution is worse when more pixels collect charge.

This paper has shown how charge sharing and weighting potential cross-talk can degrade the spectral performance, even for an ideal detectors with no consideration of material defects nor electric field non-uniformities. For many CdZnTe crystals, the measured energy resolution of common-grid detectors coupled to an ASIC will be dominated by the contribution from material defects and charge transport non-uniformities. This simulation provides a baseline in terms of device performance and shows the limit to which charge sharing and weighting potential cross-talk can degrade an ideal device. This can be used to understand what aspects of a real system depart from the expected behavior.

References

[1] F. Zhang, Z. He, C.E. Seifert, IEEE Transactions on Nuclear Science NS-54 (4) (2007) 843. doi:10.1109/TNS.2007.902354.
[2] A.E. Bolotnikov, G.C. Camarda, G.W. Wright, R.B. James, IEEE Transactions on Nuclear Science NS-52 (1) (2005) 589. doi:10.1109/TNS.2005.851419 ISSN 0018-9499.
[3] F. Zhang, Z. He, G.F. Knoll, D.K. Wehe, J.E. Berry, IEEE Transactions on Nuclear Science NS-52 (5) (2005) 2009. doi:10.1109/TNS.2005.856821 ISSN 0018-9499.
[4] I. Kuvvetli, C. Budtz-Jørgensen, Measurements of charge sharing effects in pixilated CZT/CdTe detectors, in: Nuclear Science Symposium Conference Record, 2007, NSS'07, vol. 3, IEEE, October 26, 2007–November 3, 2007, pp. 2252–2257, doi: 10.1109/NSSMIC.2007.4436596.
[5] K. Iniewski, H. Chen, G. Bindley, I. Kuvvetli, C. Budtz-Jorgensen, Modeling charge sharing effects in pixellated CZT detectors, in: Nuclear Science Symposium Conference Record, 2007, NSS'07, vol. 6, IEEE, October 26, 2007–November 3, 2007, pp. 4608–4611, doi: 10.1109/NSSMIC.2007.4437135.
[6] Z. He, W. Li, G.F. Knoll, D.K. Wehe, J. Berry, C.M. Stahle, Nuclear Instruments and Methods in Physics Research Section A: Accelerators, Spectrometers, Detectors and Associated Equipment 422 (1–3) (1999) 173. doi:10.1016/S0168-9002(98)00950-4 ISSN 0168-9002.
[7] A.E. Bolotnikov, S.O. Babalola, G.S. Camarda, H. Chen, S. Awadalla, Y. Cui, S.U. Egarievwe, P.M. Fochuk, R. Hawrami, A. Hossain, J.R. James, I.J. Nakonechnyj, J. Mackenzie, G. Yang, C. Xu, R.B. James, IEEE Transactions on Nuclear Science NS-56 (4) (2009) 1775. doi:10.1109/TNS.2009.2019960 ISSN 0018-9499.
[8] S. Agostinelli, et al., Nuclear Instruments and Methods in Physics Research Section A: Accelerators, Spectrometers, Detectors and Associated Equipment 506 (3) (2003) 250. doi:10.1016/S0168-9002(03)01368-8 ISSN 0168-9002.
[9] J. Allison, et al., IEEE Transactions on Nuclear Science NS-53 (1) (2006) 270. doi:10.1109/TNS.2006.869826 ISSN 0018-9499.
[10] Z. He, W. Li, G.F. Knoll, D.K. Wehe, Y.F. Du, Nuclear Instruments and Methods in Physics Research Section A: Accelerators, Spectrometers, Detectors and Associated Equipment 439 (2–3) (2000) 619. doi:10.1016/S0168-9002(99)00841-4 ISSN 0168-9002.
[11] Maxwell 3D. Ansoft, Four Station Square, Suite 200, Pittsburgh, PA 15219, USA.
[12] M. Amman, J.S. Lee, P.N. Luke, H. Chen, S.A. Awadalla, R. Redden, G. Bindley, IEEE Transactions on Nuclear Science NS-56 (3) (2009) 795. doi:10.1109/TNS.2008.2010402 ISSN 0018-9499.
[13] A. Pullia, S. Riboldi, IEEE Transactions on Nuclear Science NS-51 (4) (2004) 1817. doi:10.1109/TNS.2004.832564 ISSN 0018-9499.
[14] S.E. Anderson, M.L. Rodrigues, Z. He, Digital waveform analysis techniques for pixelated semiconductor detectors, in: Nuclear Science Symposium Conference Record, 2007, NSS'07, vol. 2, IEEE, October 26, 2007–November 3, 2007, pp. 1581–1586, doi: 10.1109/NSSMIC.2007.4437300.
[15] Y. Zhu, S.E. Anderson, Z. He, IEEE Transactions on Nuclear Science NS-58 (3) (2011) 1400. doi:10.1109/TNS.2011.2132738.